Rarefied flow separation in microchannel with bends

Minh Tuan Ho[1], Jun Li[2],†, Wei Su[1], Lei Wu[3], Matthew K. Borg[4], Zhihui Li[5] and Yonghao Zhang[1],†

[1]James Weir Fluids Laboratory, Department of Mechanical and Aerospace Engineering, University of Strathclyde, Glasgow G1 1XJ, UK

[2]Center for Integrative Petroleum Research, College of Petroleum Engineering and Geosciences, King Fahd University of Petroleum & Minerals, Dhahran 31261, Saudi Arabia

[3]Department of Mechanics and Aerospace Engineering, Southern University of Science and Technology, Shenzhen 518055, PR China

[4]School of Engineering, University of Edinburgh, Edinburgh EH9 3FB, UK

[5]Hypervelocity Aerodynamics Institute, China Aerodynamics Research and Development Center, Mianyang 621000, PR China

Based on an accurate numerical solution of the kinetic equation using well-resolved spatial and velocity grids, the separation of rarefied gas flow in a microchannel with double rectangular bends is investigated over a wide range of Knudsen and Reynolds numbers. Rarefaction effects are found to play different roles in flow separation (vortex formation) at the concave and convex corners. Flow separations near the concave and convex corners are only observed for a Knudsen number up to 0.04 and 0.01, respectively. With further increase of the Knudsen number, flow separation disappears. Due to the velocity slip at the solid walls, the concave (convex) vortex is suppressed (enhanced), which leads to the late (early) onset of separation of rarefied gas flows with respect to the Reynolds number. The critical Reynolds numbers for the emergence of concave and convex vortices are found to be as low as 0.32×10^{-3} and 30.8, respectively. The slip velocity near the concave (convex) corner is found to increase (decrease) when the Knudsen number increases. An adverse pressure gradient appears near the concave corner for all the examined Knudsen numbers, while for the convex corner it only occurs when the Knudsen number is less than 0.1. Due to the secondary flow and adverse pressure gradient near the rectangular bends, the mass flow rate ratio between the bent and straight channels of the same length is a non-monotonic function of the Knudsen number. Our results clarify the diversified and often contradictory observations reported in the literature about flow rate enhancement and vortex formation in bent microchannels.

Key words: micro-/nano-fluid dynamics, rarefied gas flow

1. Introduction

Gas flow in microchannels linking large reservoirs is a fundamental problem of rarefied gas dynamics underpinning the development of microsystems. Although the rarefied gas

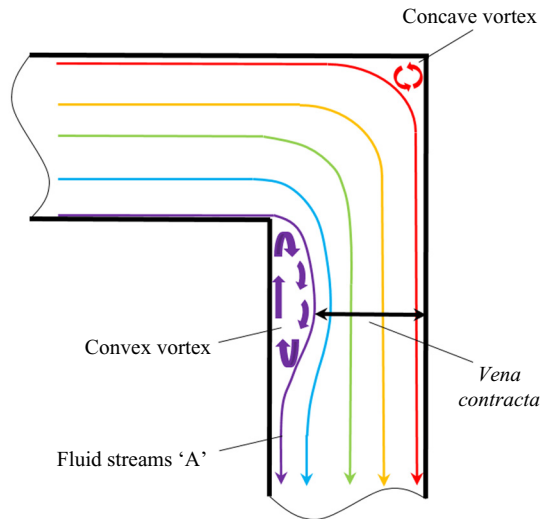† Email addresses for correspondence: junli@kfupm.edu.sa, yonghao.zhang@strath.ac.uk

FIGURE 1. Schematic of laminar flow separation (vortex formation) in a microchannel with a rectangular bend.

flow in a straight microchannel has been extensively investigated (Sharipov & Seleznev 1998; Sazhin 2009; Titarev 2012*a*,*b*; Varoutis, Day & Sharipov 2012), only a few experimental (Lee, Wong & Zohar 2001; Varade *et al.* 2015) and numerical (Raju & Roy 2004; Wang & Li 2004; Agrawal, Djenidi & Agrawal 2009; Sharipov & Graur 2012; White *et al.* 2013; Kulakarni, Shterev & Stefanov 2015; Rovenskaya 2016; Liu *et al.* 2018) studies have been carried out for rarefied gas flows through a microchannel with bends, which are often encountered in miniaturised devices. One of the typical phenomena in bent channels is flow separation, which is important for many engineering applications and has been studied extensively in the continuum limit (Bradshaw & Wong 1972). In the literature, flow recirculation, vortex formation or secondary flow is also often used to describe flow separation phenomena. However, much less attention has been paid to flow separation in microsystems, as the Reynolds number *Re* is often small. Moreover, the Knudsen number *Kn*, which is defined as the ratio between the mean free path of gas molecules and the characteristic flow length, is not always small, resulting in a new mechanism for flow separation which does not appear in macrosystems. For example, in an early work on gas flow separation in a bent microchannel (Lee *et al.* 2001), the experimentally measured data at a fixed Knudsen number at the channel exit ($Kn_e = 0.06$) showed that the mass flow rate ratio between the bent and straight channels of the same length, i.e.

$$\alpha = \frac{G_{bent}}{G_{straight}} \tag{1.1}$$

is close to 0.8, when the pressure ratio

$$\beta = \frac{p_e}{p_i}, \tag{1.2}$$

between the exit and the inlet varies from 0.25 to 0.33. Moreover, the pressure gradients around the concave and convex corners are nearly zero and positive, respectively, indicating that the flow separation or vortex generation at both corners, as illustrated in figure 1, may exist even at very low Reynolds numbers, i.e. $Re \leq 0.06$. This critical value

of Reynolds number is three orders of magnitude smaller than the lowest Reynolds number (approximately 100 to 300) in the continuum flow for the emergence of flow separation (Maharudrayya, Jayanti & Deshpande 2004; Xiong & Chung 2008).

The pioneering experimental work of Lee *et al.* (2001) inspired the numerical investigations to understand rarefied gas flow in bent microchannels, but many contradictory results are reported, which are summarised in table 1. Flow separation at the concave corner is, surprisingly, captured by Agrawal *et al.* (2009), White *et al.* (2013) and Varade *et al.* (2015) at low Reynolds numbers using the lattice Boltzmann method, the direct simulation Monte Carlo (DSMC) method (Bird 1994) and the Navier–Stokes solver, respectively. Small recirculation at the bends can be deduced from the velocity profiles obtained in the numerical simulation of the Navier–Stokes equations with the first-order slip velocity boundary condition (Raju & Roy 2004). However, the others explicitly confirmed that no trace of flow separation was found using the DSMC method (Wang & Li 2004) and the discrete velocity method (DVM) of solving the linearised kinetic equations (Sharipov & Graur 2012; Liu *et al.* 2018).

Table 1 further shows that the mass flow rate ratio α is reported in the literature in a rather scattered fashion. Raju & Roy (2004) showed that α varies from 0.38 to 0.52 when the pressure ratio β is increased and Kn_e is fixed around 0.06. The others reported that α is very close to unity or slightly higher than unity in the slip flow regime. Also, it varies differently with respect to the Knudsen number: Liu *et al.* (2018) reported that α decreases monotonically when Kn increases; White *et al.* (2013) found the steep increase of α to its maximum value at the inlet Knudsen number of $Kn_i = 0.027$, followed by a gradual decrease; Agrawal *et al.* (2009) and Rovenskaya (2016) observed a steep increase of α to its maximum value at $Kn_e = 0.2$ and 0.05, then remaining plateaued up to $Kn_e = 0.5$ and 0.1, respectively. This small flow rate enhancement in the bent channel compared with the straight channel has been attributed to numerical uncertainty (Agrawal *et al.* 2009), reduction of average shear stress (White *et al.* 2013; Rovenskaya 2016) or cross-section expansion at the bends (Liu *et al.* 2018). As no vortex is found in the detailed flow structure analysis, the case of flow rate ratio α less than unity is attributed to rarefaction effect rather than flow separation (Wang & Li 2004). On the other hand, when the exit Knudsen number is fixed at $Kn_e \approx 0.06$, the mass flow rate ratio α increases considerably with the pressure ratio β (Raju & Roy 2004), which contradicts the experimental observation of the constant ratio (Lee *et al.* 2001).

It is the aim of the present work to elucidate the contradictory findings on flow separation and flow rate enhancement due to bent channels through a thorough numerical study covering a wide range of Knudsen numbers and Reynolds numbers. To ensure computational accuracy, the kinetic equation is solved by the deterministic DVM with very refined spatial resolution.

2. Problem statement and gas kinetic simulation

2.1. *Statement of the problem*

Consider the rarefied flow of argon gas through the straight and bent channels of the same height h and axis length $L_{ch} = 5h$ connecting the two reservoirs of equal size, see figure 2. The gas pressures in the upstream and downstream reservoirs are p_i and p_e, respectively. The reservoir gas and wall temperatures are kept at $T_0 = 273$ K. The resulting rarefied gas flow is characterised by the pressure ratio β and the reference Knudsen number

$$Kn = \frac{\lambda}{L_0}, \quad \lambda = \frac{\mu_0}{p_0}\sqrt{\frac{\pi k_B T_0}{2m}}, \quad (2.1a,b)$$

Reference	Vortex	Re	Kn range		α	β
			all	maximum α		
Lee et al. (2001)	E	≤ 0.06	fixed 0.06_e	*	0.8	$0.25 \sim 0.33$
Varade et al. (2015)	Yes	$0.27 \sim 418.5$	$0.0003 \sim 0.0385_e$	$0.005 \sim 0.02_m$	$0.45 \sim 0.95$	N.A.
Raju & Roy (2004)	E	≤ 0.04	fixed 0.0585_e	**	$0.38 \sim 0.52$	$0.37 \sim 0.75$
Wang & Li (2004)	No	≤ 15	fixed 0.062_e	N.A.	N.A.	$0.33 \sim 0.5$
Agrawal et al. (2009)	Yes	$2.14 \sim 19.3$	$0.060 \sim 1_e$	$0.2 \sim 0.5_e$	$0.99 \sim 1.01$	0.33
Sharipov & Graur (2012)	No	N.A.	$0.009 \sim 88.6_m$	***	$0.31 \sim 1.18$	≈ 1
White et al. (2013)	Yes	$0.18 \sim 27.9$	$0.011 \sim 0.30_i$	0.027_i	$0.95 \sim 1.02$	0.33
Kulakarni et al. (2015)	N.M.	N.A.	$0.089 \sim 0.89_m$	N.A.	N.A.	$0.33 \sim 0.5$
Rovenskaya (2016)	N.M.	$1.41 \sim 73.77$	$0.01 \sim 0.1_e$	$0.05 \sim 0.1_e$	$0.94 \sim 1.02$	$0.16 \sim 0.48$
Liu et al. (2018)	No	N.A.	$0.00 \sim 10_m$	***	$0.62 \sim 1.03$	≈ 1

TABLE 1. Contradictory reports in the literature about existence of vortex in microchannels and mass flow rate ratio α. Here, *: α is almost constant with increasing pressure ratio β; **: α increases monotonically with increasing pressure ratio β; ***: α decreases monotonically with increasing mean Knudsen number Kn_m. Subscripts 'i', 'e' and 'm' in the Kn range indicate the inlet, exit and mean Knudsen number, respectively. Abbreviations 'E', 'N.M.' and 'N.A.' mean 'expected', 'not mentioned' and 'not available', respectively.
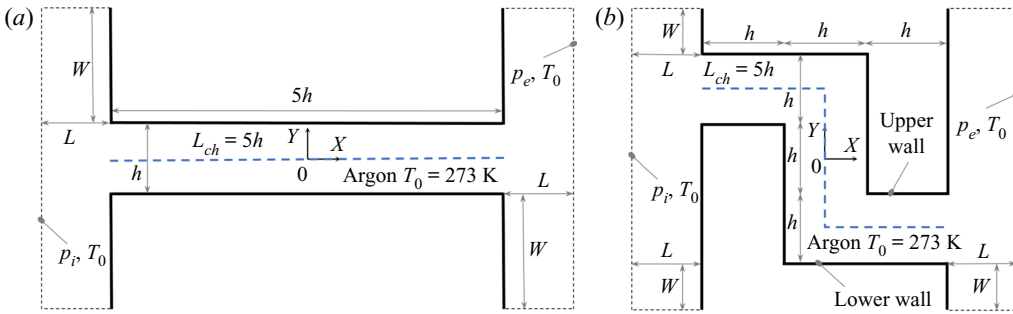
FIGURE 2. Pressure-driven gas flow from the left-hand reservoir to the right-hand reservoir through (*a*) the straight channel and (*b*) the bent channel of the same height *h* and axis length $L_{ch} = 5h$. Note that only part of the reservoirs are illustrated here.

where μ_0, λ, m and k_B are the gas viscosity at temperature T_0, the molecular mean free path, the molecular mass and the Boltzmann constant, respectively. The channel height and the inlet pressure are taken as the reference length $L_0 = h$ and the reference pressure $p_0 = p_i$, respectively. As a result, our reference Knudsen number is the inlet Knudsen number $Kn = Kn_i$. When the exit or mean Knudsen number (Kn_e or Kn_m) is of interest, it can be calculated from the reference Knudsen number and pressure ratio β, i.e. $Kn_e = Kn/\beta$ or $Kn_m = Kn(1 + \beta)/(2\beta)$, respectively. Alternatively, the gas rarefaction can be characterised by the rarefaction parameter δ, which relates to Kn as $\delta = \sqrt{\pi}L_0/2\lambda = \sqrt{\pi}/2Kn$.

The effect of pressure ratio can be reflected by the Reynolds number *Re* that is defined as

$$Re = \frac{\rho_0 U_0 L_0}{\mu_0}, \tag{2.2}$$

where U_0 is the characteristic flow speed, e.g. the average speed in the channel and $\rho_0 = mp_0/(k_B T_0)$ is the reference density. The Mach number *Ma* relates to the Knudsen number *Kn* and the Reynolds number *Re* through the von Kármán relation

$$Ma = \sqrt{\frac{2}{\pi\gamma}}KnRe, \tag{2.3}$$

where the specific heat ratio γ is taken to be 5/3 for monatomic gas.

2.2. *The governing equation and boundary condition*

The Boltzmann equation is the fundamental equation to describe the rarefied dynamics of monatomic gas. However, due to the complexity of its collision operator, the kinetic model (Shakhov 1968) is often used to simulate rarefied gas flows. Without an external body force, the Shakhov model equation takes the following form:

$$\frac{\partial f}{\partial t} + c \cdot \nabla f = \frac{f^S - f}{\tau}. \tag{2.4}$$

Here $f = f(x, c, t)$ is the velocity distribution function of gas molecules with molecular velocity $c = (c_x, c_y, c_z)$ at position $x = (x, y, z)$ and time t, and the reference distribution

function f^S reads

$$f^S = \frac{n}{(2\pi k_B T/m)^{3/2}} \exp\left(-\frac{m\xi^2}{2k_B T}\right)\left[1 + (1 - Pr)\frac{m\boldsymbol{\xi} \cdot \boldsymbol{q}}{5n\,(k_B T)^2}\left(\frac{m\xi^2}{k_B T} - 5\right)\right], \quad (2.5)$$

where n and T are the gas number density and temperature, respectively, $\boldsymbol{\xi} = \boldsymbol{c} - \boldsymbol{u}$ is the peculiar velocity, with $\boldsymbol{u}$ the macroscopic flow velocity and $\boldsymbol{q} = (m/2)\int \boldsymbol{\xi}\xi^2 f\,d\boldsymbol{c}$ is the heat flux. The Prandtl number Pr is set to be $2/3$ for monatomic gas. Conservative flow variables are calculated as $\boldsymbol{W} \equiv (n, n\boldsymbol{u}, ne)^T = \int (1, \boldsymbol{c}, c^2/2)^T f\,d\boldsymbol{c}$ and the temperature is determined from the specific total energy $e = (u^2 + 3k_B T/m)/2$.

The relaxation time τ in the Shakhov model (2.4) is related to the dynamic viscosity μ and the local pressure p as $\tau = \mu/p = \mu/(nk_B T)$. For gas molecules interacting through the inverse power law potential, the dynamic viscosity μ depends on the temperature T as

$$\mu = \mu_0\left(\frac{T}{T_0}\right)^{\omega}, \quad (2.6)$$

where ω is the viscosity index. Argon gas with $m = 6.63 \times 10^{-26}$ kg, $\mu_0 = 2.117 \times 10^{-5}$ Ns m^{-2} and $\omega = 0.81$ is considered in this paper.

To simulate the rarefied gas flow, the gas–surface interaction should be specified, which is modelled by the Maxwell diffuse–specular reflection, i.e.

$$f(\boldsymbol{c} \mid \boldsymbol{c} \cdot \boldsymbol{N} > 0) = \alpha_d n_s \left(\frac{m}{2\pi k_B T_0}\right)^{3/2} \exp\left(-\frac{mc^2}{2k_B T_0}\right)$$
$$+ (1 - \alpha_d)f\,[\boldsymbol{c} - 2\boldsymbol{N}(\boldsymbol{c} \cdot \boldsymbol{N})], \quad (0 \leq \alpha_d \leq 1), \quad (2.7)$$

where $\boldsymbol{N}, n_s, \alpha_d$ are the normal unit vector of the solid surface, the gas number density on the solid surface and the accommodation coefficient, respectively. In the diffuse–specular model, α_d portion of incident particles are reflected diffusively, whereas the remaining $(1 - \alpha_d)$ portion of incident particles have a specular reflection. The diffuse boundary condition $\alpha_d = 1$ at the solid surfaces is used in this study, except for the simulations in § 3.2 where diffuse–specular reflection is used. The gas number density on the solid surface is computed from the non-penetration condition, i.e. the number of gas molecules reflected from the wall is equal to those molecules approaching the same wall

$$n_s = -2\sqrt{\frac{\pi}{2k_B T_0/m}} \int_{\boldsymbol{c}\cdot\boldsymbol{N}<0} \boldsymbol{c} \cdot \boldsymbol{N}f\,d\boldsymbol{c}. \quad (2.8)$$

At the free surfaces of reservoirs, molecules entering the computational domain follow the Maxwellian distribution with the local bulk velocity $\boldsymbol{u}$, pressure and temperature corresponding to each reservoir. The local velocity $\boldsymbol{u}$ at the free surfaces is extrapolated from that of the interior neighbour grid points.

2.3. *The numerical methods*

We employ the reference length L_0, temperature T_0, pressure p_0 and the most probable molecular speed $v_m = \sqrt{2k_B T_0/m}$ to normalise the following variables:

$$\left(\tilde{X}, \tilde{Y}\right) = \frac{(X, Y)}{L_0}, \quad (\tilde{u}, \tilde{v}) = \frac{(u, v)}{v_m}, \quad \tilde{T} = \frac{T}{T_0}, \quad \tilde{p} = \frac{p}{p_0}, \quad \tilde{n} = \frac{n}{p_0/k_B T_0}, \quad (2.9a\text{–}e)$$

where u and v are the velocity components of macroscopic velocity $\boldsymbol{u}$ along the coordinate axes X and Y, respectively. Hereafter, the tildes on these dimensionless quantities are omitted for simplicity.

The DVM is one of the most commonly used deterministic approaches to solving the Boltzmann equation and its simplified models (Broadwell 1964; Yang & Huang 1995). It projects the continuous molecular velocity space $\boldsymbol{c}$ into a set of discrete velocities $\boldsymbol{c}^{(i)}$ ($i = 1, 2, \ldots, N_c$). As a result, the governing equation (2.4) is replaced by a system of N_c independent equations. Here, we discretise this system in time by a time-implicit Godunov-type scheme (Yang & Huang 1995; Titarev 2007)

$$
\left.
\begin{array}{l}
\left[\dfrac{1}{\Delta t^{(j)}} + \boldsymbol{c}^{(i)} \cdot \boldsymbol{\nabla} + \dfrac{1}{\tau^{(j)}} \right] \Delta f^{(j)} = \text{RHS}^{(j)}, \\[3mm]
\text{RHS}^{(j)} = \dfrac{1}{\tau^{(j)}} \left[f_{eq}^{(j)} - f^{(j)} \right] - \boldsymbol{c}^{(i)} \cdot \boldsymbol{\nabla} f^{(j)},
\end{array}
\right\}
\tag{2.10}
$$

where $\Delta f^{(j)} = f^{(j+1)} - f^{(j)}$ needs to be determined at the time step $\Delta t^{(j)}$ and j is the time step index. Here, $\text{RHS}^{(j)}$ is the explicit part, and the spatial derivative is approximated by a third-order upwind scheme. This time-implicit scheme allows us to use a large time step to accelerate steady-state solution. Specifically, the classical Courant–Friedrichs–Lewy number of 10^6 is chosen in this study. A few efficient implicit methods for solving the linearised Shakhov model have been developed by Titarev (2012a,b, 2013). The details of the DVM algorithm used in this work can be found in Ho *et al.* (2019). In the following simulations, the polar velocity grids of $N_c = N_{c_p} \times N_\varphi = 4 \times 120$ and 4×40 are chosen for $Kn > 0.1$ and $Kn \leq 0.1$, respectively. The number of discretised velocities in the angular coordinate N_φ is uniformly spaced on $[0, 2\pi]$, whereas the number of discretised velocities in the radial coordinate N_{c_p} follows the half-range Gauss–Hermite abscissae. The molecular velocity is cut off at 2.3 times the most probable molecular speed v_m with $N_{c_p} = 4$. In the cases of small pressure ratio, i.e. $\beta = 0.75, 0.5$ and low Knudsen number $Kn \leq 0.03$, $N_{c_p} = 8$ and the truncated molecular velocity of $3.7 v_m$ are used due to relatively high Mach number. With these sets of the velocity grids, the numerical uncertainty is of the order of 0.1 % when N_{c_p} is doubled (note: the truncated molecular velocity is also enlarged accordingly).

Different uniform spatial grids are used in DVM simulations based on the value of Knudsen number, i.e. $L10W4h160$, $L20W8h80$ and $L40W16h40$ are used for $Kn \leq 0.1$, $0.1 < Kn \leq 1$ and $1 < Kn$, respectively. Here, for example, the spatial grid $L10W4h160$ denotes the reservoirs are of size of $L = 10h$, $W = 4h$ and the reference length (i.e. the channel height h) is resolved by 160 uniform-cells, see figure 2.

Our simulations start from the global equilibrium state. The convergence criterion for the steady-state is checked every time step as follows:

$$
E(t) = \frac{\sum |\boldsymbol{u}(t) - \boldsymbol{u}(t - \Delta t)|}{\sum |\boldsymbol{u}(t)|} < 10^{-6}.
\tag{2.11}
$$

The reduced mass flow rate G, normalised by $h^2 (p_i - p_e)/v_m L_{ch}$, reads

$$
G = \frac{L_{ch}}{h} \frac{2 p_0}{(p_i - p_e)} \int n u \, \mathrm{d}Y = \frac{L_{ch}}{h} \frac{2 p_0}{(p_i - p_e)} u_{avg}.
\tag{2.12}
$$

The average speed $u_{avg} = \int n u \, \mathrm{d}Y$ is calculated at two vertical cross-sections inside the channel near the inlet and the exit to guarantee the mass conservation. The discrepancy of

u_{avg} near the inlet and the exit is less than 0.01 %. To calculate the Reynolds number, the characteristic flow speed U_0 in (2.2) is determined by $U_0 = u_{avg}v_m$.

In this study, DVM is used for solving the nonlinear Shakhov model, see (2.4) and (2.5) for all the values of pressure ratio β, except for $\beta = 0.99999$. For $\beta = 0.99999$, the DVM simulation converges very slowly and requires a very fine spatial grid at such low Kn (Valougeorgis & Naris 2003; Wang *et al.* 2018). Therefore, the discontinuous Galerkin method (DGM) and general synthetic iterative scheme, which enables the fast convergence to the steady-state solution and retains asymptotic preserving natures of the Navier–Stokes equations, is employed to solve the linearised Shakhov equation for the case of pressure ratio $\beta = 0.99999$ (Su *et al.* 2019*b*, 2020*b*). The DVM and DGM solutions are compared with each other and with the other available data, see appendix A.

3. Flow separation at bends

In this section, we numerically investigate the gas flow through the bent channel over a wide range of Knudsen and Reynolds numbers. In particular, the role of velocity slip on the flow separation (vortex formation) is evaluated.

3.1. *Influence of Reynolds number and Knudsen number*

In our simulations, the Knudsen number Kn and the pressure ratio β are chosen first, and the Reynolds number Re is then obtained from the simulation results. The compressibility of the gas tends to suppress vortices generation which has been observed in supersonic flows, e.g. see Burggraf (1966). The compressibility effects may be insignificant as the Mach number Ma calculated from the von Kármán relation (2.3) is up to 1.5×10^{-3}, 1.5×10^{-2}, 0.19 and 0.25 for all the considered cases of the pressure ratio $\beta = 0.99999$, 0.99, 0.75 and 0.5, respectively.

Figure 3 shows the streamlines and the pressure distribution inside the bent channel for $Kn = 0.01$, 0.02 and 0.05 with the pressure ratio $\beta = 0.99$ and 0.5. With the fixed pressure ratio β and increasing Kn, Re becomes smaller so that the vortices at the bends shrink or even disappear. The strong influence of Re, i.e. the inertial effect from the mainstream, on the vortex formation is well known for continuum flows; however, with the presence of gas rarefaction effect in microflow, two unusual phenomena are observed in figure 3. First, the Reynolds number alone cannot characterise the flow separation in a microchannel. For example, from figures 3(*c*) and 3(*f*) we see that in the slip flow regime the vortices exist at $Re = 0.68$ but not at a larger Re of 4.72. Second, as shown in figures 3(*c*) and 3(*b*), the vortices near the concave and convex corners occur at Re as small as 0.68 and 40.65, respectively, while the corresponding critical Reynolds numbers (i.e. the smallest Re where the vortex emerges) for air in the continuum flow regime, obtained from the Navier–Stokes equations with a no-slip boundary condition (Maharudrayya *et al.* 2004), are 200 and 100; on the other hand, for water flow in a microchannel no vortex is observed experimentally when $Re < 100$ (Xiong & Chung 2008). To analyse these contradictory observations, we need to look into the secondary flows at the bends.

To the best of authors' knowledge, the concave vortex, which exists near the concave corners, is closely related to the Moffatt eddies originally found by the Stokes stream function for viscous fluid near deep sharp corners in Stokes flow (Moffatt 1964). Contrary to the conventional vortex occurring at high Re, where the centrifugal force is balanced by the pressure force, the Moffatt viscous vortex is both driven and damped by the viscous force. By solving the stream function in the Stokes limit at the vicinity of a sharp corner, Moffatt found that a sequence of vortices generally appears if the angle of the sharp corner
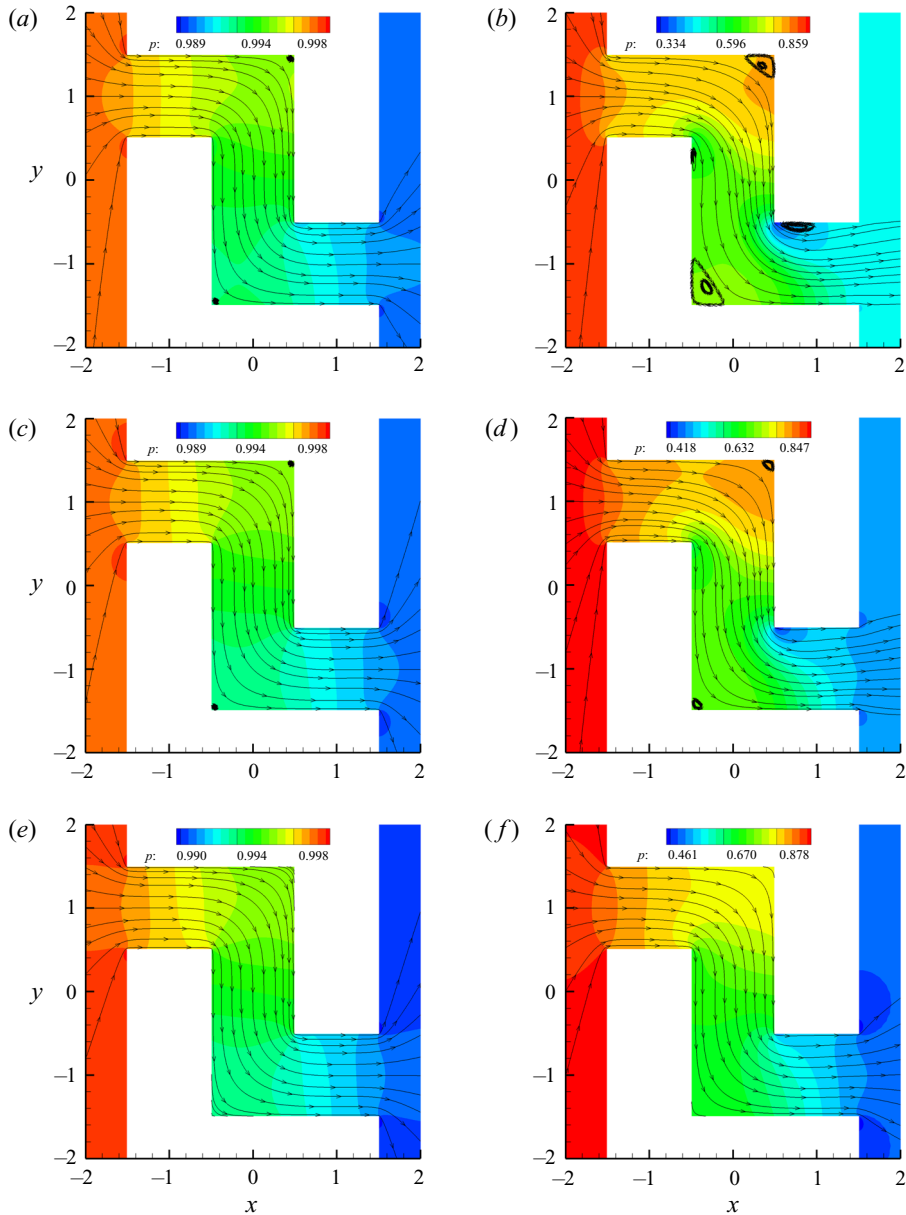
FIGURE 3. The pressure field and streamlines of rarefied argon gas flow inside the bent channel at different values of Kn and Re. Note: the rarefaction δ of 88.6, 44.3, 17.7 corresponds to $Kn = 0.01, 0.02, 0.05$, respectively. (*a*) $\beta = 0.99, Kn = 0.01, Re = 2.48$; (*b*) $\beta = 0.5, Kn = 0.01, Re = 40.65$; (*c*) $\beta = 0.99, Kn = 0.02, Re = 0.68$; (*d*) $\beta = 0.5, Kn = 0.02, Re = 17.80$; (*e*) $\beta = 0.99, Kn = 0.05, Re = 0.13$ and (*f*) $\beta = 0.50, Kn = 0.05, Re = 4.72$.

is smaller than the critical angle $146°$. In the hydrodynamic regime, Moffatt eddies have been confirmed numerically by Biswas, Breuer & Durst (2004) in backward-facing step flows, where the primary vortex has been observed in a wide range of Re from 10^{-4} to 10^2. Interestingly, the vortex size is nearly constant when the Reynolds number increases up to
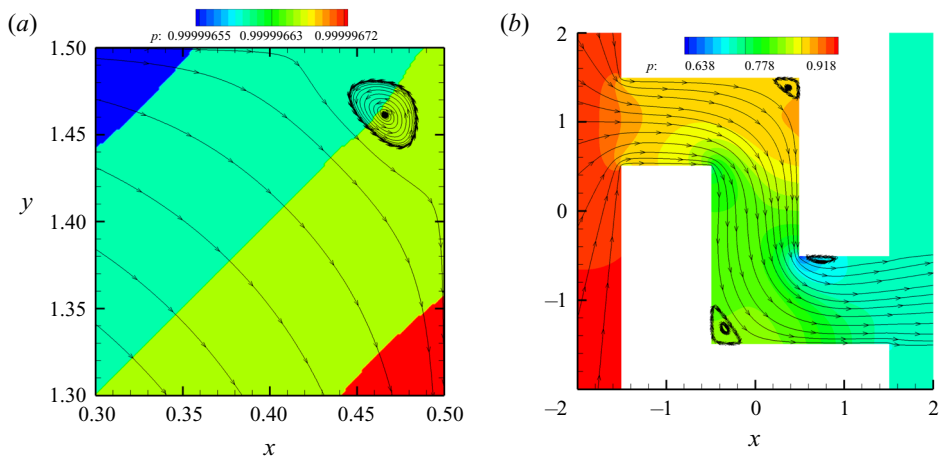
FIGURE 4. Critical values of the Reynolds number for the emergence of (*a*) concave vortex (enlarged view of the pressure field and streamlines near the first concave corner of the upper wall) and (*b*) convex vortex. Note: the rarefaction δ of $88.6, 29.5$ corresponds to $Kn = 0.01, 0.03$, respectively. (*a*) $Re = 0.32 \times 10^{-3}$, $Kn = 0.03$, $\beta = 0.99999$ and (*b*) $Re = 30.8$, $Kn = 0.01$, $\beta = 0.75$.

unity, then becomes larger with a further increase of Re (up to 100). Also, the size ratio of the primary vortex to the secondary vortex obtained by their Navier–Stokes simulations for $Re = 1$ is in good agreement with the Stokes approximation in the Moffatt analysis (16.28 for the right angle corner). This rapid reduction of the size of successive vortices leads to enormous difficulty in capturing a sequence of vortices experimentally. In gas microflow, the concave vortex was, surprisingly, observed in the numerical simulations with Re of the order of unity (Agrawal *et al.* 2009; White *et al.* 2013). Without awareness of Moffatt's theory, the existence of a concave vortex at such low Re is either attributed to gas rarefaction (Agrawal *et al.* 2009) or not acknowledged (Wang & Li 2004; Sharipov & Graur 2012; Liu *et al.* 2018). We observe, for the first time, that the concave vortex in gas microflows does exist in the limit as the Reynolds number approaches zero, which agrees with Moffatt's theory. From our simulations, the smallest Reynolds number for a vortex to appear is found to be 0.32×10^{-3} for the case of pressure ratio $\beta = 0.99999$ and $Kn = 0.03$, as shown in figure 4(*a*).

The convex vortex, which appears in the downstream side of convex bent corners, is formed when the fluid streams cannot move closely along the sharp angle of the wall after the convex corner due to their relatively high momentum. The flow separation emerges from the convex corner point and extends beyond the *vena contracta*, i.e. the narrowest region of the stream after a sudden contraction of the duct (see the schematic diagram in figure 1). A similar effect is also observed in the slip flow through an orifice (Sharipov 2004; Ho & Graur 2014). This type of vortex was observed clearly from the experiments of water flow through a microchannel with bends at $Re \geq 300$ (Xiong & Chung 2008). To the best of the authors' knowledge, this is the first study that detects this type of vortex for rarefied gas flow at a much smaller Reynolds number compared with continuum flow. From our simulations, the smallest Reynolds number for the emergence of a convex vortex is found to be 30.8 in the case of pressure ratio $\beta = 0.75$ and $Kn = 0.01$, in which a single convex vortex occurs near the second rectangular bend as shown in figure 4(*b*).

3.2. *Influence of velocity slip*

To understand the puzzling behaviour of concave and convex vortices for rarefied gas flows at low Reynolds number, we analyse the influence of velocity slip at the channel surface, which is one of the major rarefaction effects when *Kn* is small. Note that when the other parameters are fixed, the smaller the accommodation coefficient α_d is, the larger the slip velocity will be (Loyalka 1968; Su *et al.* 2019*a*). Here, we change α_d and keep both *Kn* and β fixed to allow significant variation of slip velocity u_s at the wall while the mainstream velocity is only slightly affected. For example, in the following two cases the Reynolds numbers are changed by less than 5 % and 0.9 % when α_d is varied from 1 to 0.6.

The influence of slip velocity on the flow field near the concave corner is shown in figure 5, when $Kn = 0.01$ and $\beta = 0.99$. It can be seen from figures 5(*a*) and 5(*b*) that, when α_d decreases (i.e. the slip velocity increases), the size of the vortex shrinks and its core centre moves towards the corner. Slip velocity profiles along the upper and lower walls, as shown in figures 5(*c*) and 5(*d*), demonstrate that no slip exists in the region near the concave corner (i.e. at $d/h \approx 2$ of the upper wall and $d/h \approx 3$ of the lower wall, where *d* is the distance between the inlet of a microchannel and the considered point along the corresponding wall) and this non-slip region increases with α_d. This can be explained by the fact that, when α_d decreases, the induced larger slip velocity needs a longer distance to reduce to zero at the concave corner. As a consequence, the wall surface with no-slip flow becomes smaller and the Moffatt vortex is suppressed at a lower α_d. A weak adverse pressure gradient is also found at the concave corner region, see figures 5(*e*) and 5(*f*).

The influence of slip velocity on the flow field at the convex corner is presented in figure 6, when $Kn = 0.01$ and $\beta = 0.5$. In contrast to the concave vortex, the convex vortex is larger and its core centre moves away from the corner point when α_d decreases from 1 to 0.6, see figures 6(*a*) and 6(*b*). This can be explained by the fact that fluid streams, denoted as fluid streams 'A' in figure 1, departing from the upstream wall of the corner cannot follow a sharp rectangular turn and are separated from the downstream wall of the corner. These separations create a fluid region between the downstream wall of the corner and the separated streams 'A'. As no fluid stream departing from the inlet can access this region, a recirculation occurs, resulting in the vortex in this region. Fluid streams 'A', through viscous force, drive the convex vortex. As the speed of fluid streams 'A' increases with reduction of α_d – see the slip velocity at the convex corner ($d/h = 4$ for the upper wall and $d/h = 1$ for the lower wall) shown in figures 6(*c*) and 6(*d*) – the convex vortex becomes larger. A larger vortex leads to a shortened *vena contracta*. When α_d decreases, the slip velocity of backward flow and separation length (from the corner point to the reattachment point) increases. The sudden jump and drop of slip velocity can also be seen at the convex corner, which is positively related to the abrupt drop of pressure profile along the wall before the convex corner shown in figures 6(*e*) and 6(*f*). An adverse pressure gradient along the wall after the convex corner is consistent with the pressure field near the convex corner as shown in figures 6(*a*) and 6(*b*). The adverse pressure gradient after the convex corner is significantly stronger than that at the concave corner ($d/h = 2$ for the upper wall and $d/h = 3$ for the lower wall), this can also be seen for the case shown in figure 5.

3.3. *Explanation of separation in rarefied gas flows*

From the above numerical simulations, we know that the slip velocity suppresses flow separation at the concave corner and intensifies flow separation at the convex corner. This finding can explain the two unusual observations of rarefied flow separation presented in § 3.1. First, the momentum of bulk fluid is much larger in the case shown in figure 3(*f*)
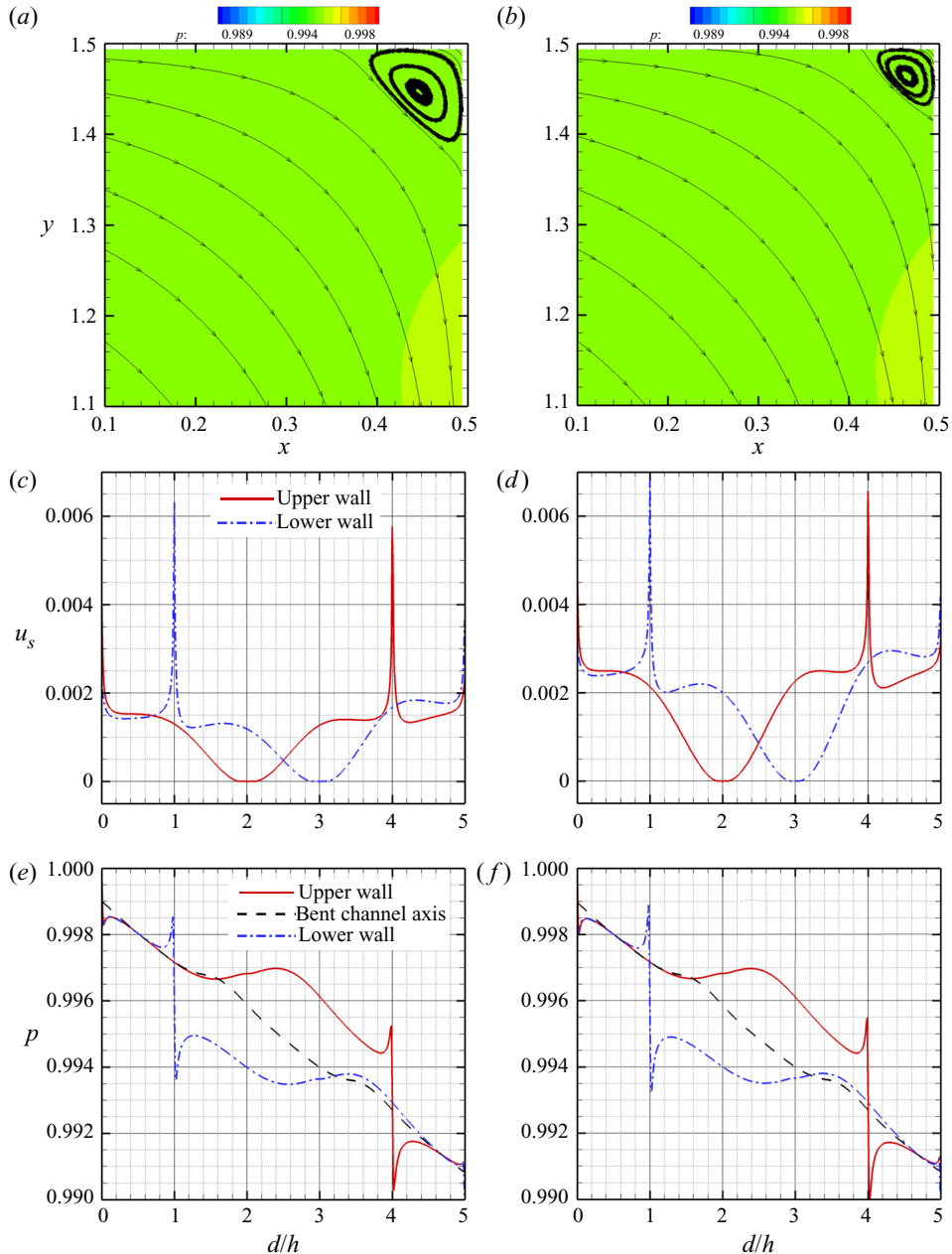
FIGURE 5. Vortex, slip velocity and adverse pressure gradient at the concave corner when $Kn = 0.01$, $\beta = 0.99$. (*a* and *b*) Enlarged view of the pressure field and streamlines near the first concave corner (upper wall); (*c* and *d*) the slip velocity along the upper and lower walls; (*e* and *f*) the pressure along the upper and lower walls, and the channel axis. The distance d is measured from the inlet of the microchannel along the upper wall, the lower wall or the channel axis, so that the concave corner is positioned at $d/h = 2$ and 3 for the upper and lower walls, respectively. The Reynolds numbers are 2.48 and 2.60 for $\alpha_d = 1$ and $\alpha_d = 0.6$, respectively. (*a*) $\alpha_d = 1$, the first concave corner; (*b*) $\alpha_d = 0.6$, the first concave corner; (*c*) $\alpha_d = 1$, slip velocity profile; (*d*) $\alpha_d = 0.6$, slip velocity profile; (*e*) $\alpha_d = 1$, pressure profile and (*f*) $\alpha_d = 0.6$, pressure profile.
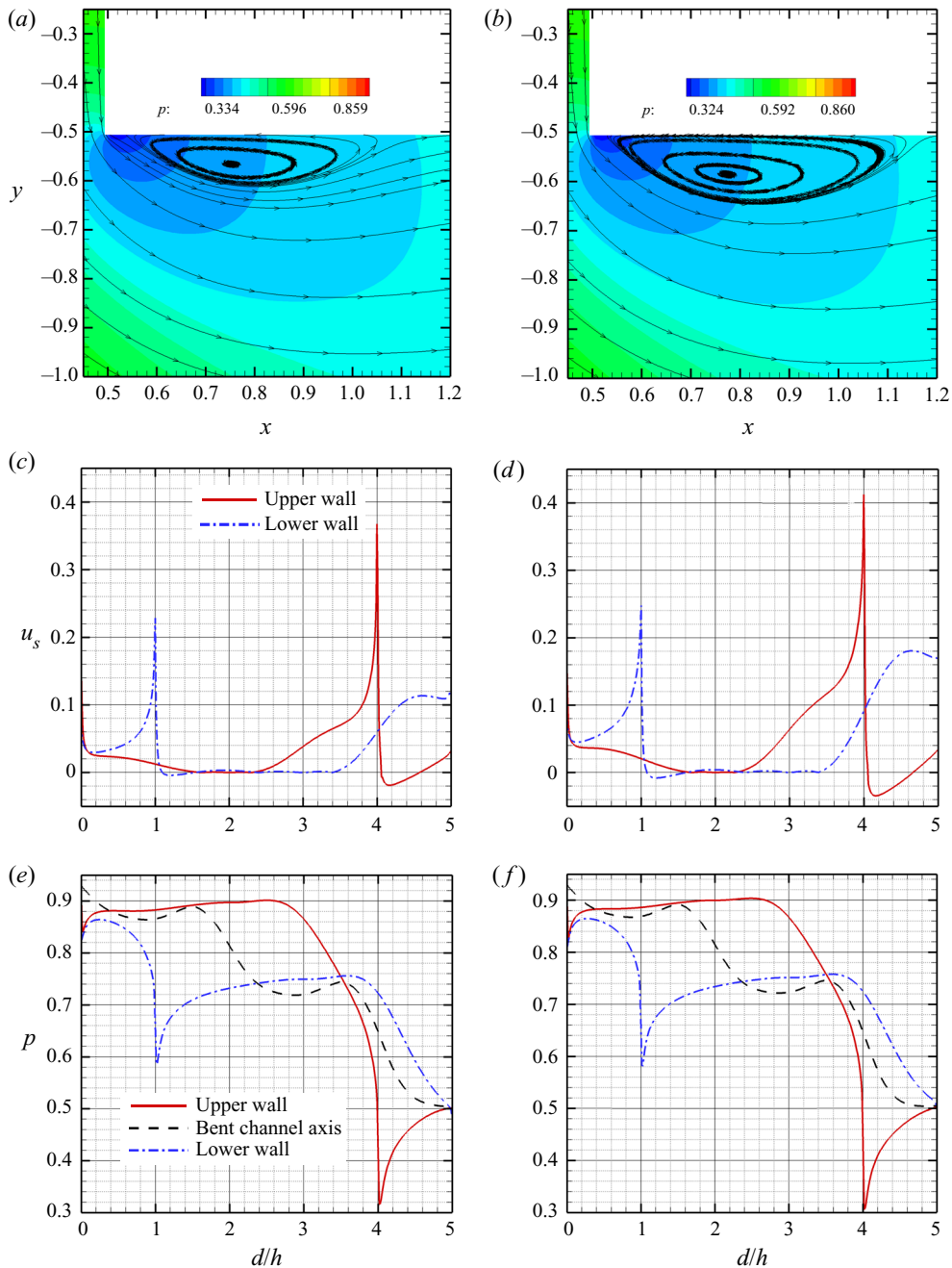
FIGURE 6. Vortex, slip velocity and adverse pressure gradient at the convex corner when $Kn = 0.01$, $\beta = 0.5$: (*a* and *b*) Enlarged view of the pressure field and streamlines near the second convex corner (upper wall); (*c* and *d*) the slip velocity along the upper and lower walls; (*e* and *f*) the pressure along the upper wall, the lower wall, and the channel axis. The convex corner is positioned at $d/h = 4$ and 1 for the upper and lower walls, respectively. The Reynolds numbers are 40.65 and 41.01 for $\alpha_d = 1$ and $\alpha_d = 0.6$, respectively. (*a*) $\alpha_d = 1$, the second convex corner; (*b*) $\alpha_d = 0.6$, the second convex corner; (*c*) $\alpha_d = 1$, slip velocity profile; (*d*) $\alpha_d = 0.6$, slip velocity profile; (*e*) $\alpha_d = 1$, pressure profile and (*f*) $\alpha_d = 0.6$, pressure profile.
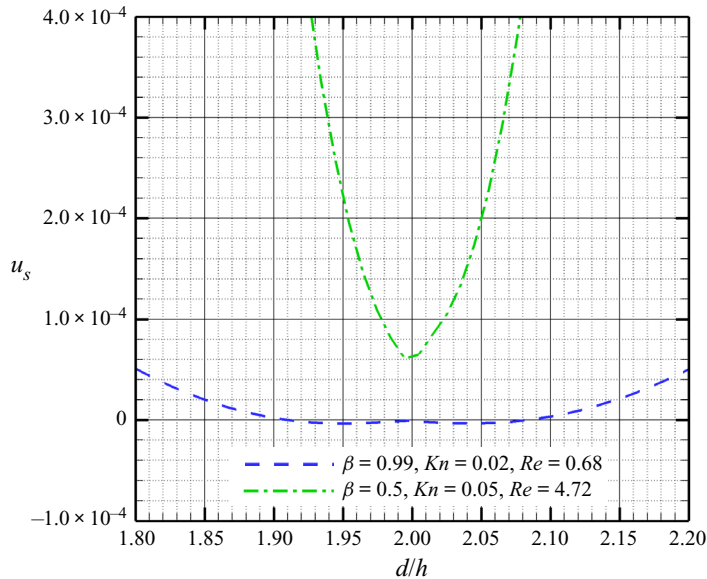
FIGURE 7. Slip velocity near the first concave corner (the upper wall, $d/h = 2$) for the cases shown in figures 3(*c*) and 3(*f*). The distance *d* is measured along the upper wall, starting from the inlet of the microchannel.

than that in figure 3(*c*), however, flow separation is not observed in figure 3(*f*). This is because the Moffatt vortex is suppressed by a significant increase of the slip velocity at the concave corner for $Kn = 0.05$, see figure 7. As the size of the Moffatt vortex is significantly reduced in rarefied flow, it is more difficult to capture in simulations and experiments. This explains why the Moffatt vortex was not detected in some numerical studies of rarefied gas flow in bent microchannels (Wang & Li 2004; Sharipov & Graur 2012; Liu *et al.* 2018), but was captured by others with much refined grids (Agrawal *et al.* 2009; White *et al.* 2013; Varade *et al.* 2015). Second, the velocity slip in gas rarefied flows enhances the convex vortex leading to 'early onset' of flow separation in microsystems (with respect to the Reynolds number) compared with the flow in macrosystems, in which no-slip boundary condition is applied at the fluid–wall interface. The convex vortex in a rarefied gas can be found at Reynolds numbers as small as 30.8, see figure 4(*b*).

The attenuation of vortices near a bend with increasing *Kn* at fixed pressure ratio β, as shown in figure 3, can be interpreted by the reduction of *Re*, which is consistent with the findings in the continuum flow (Agrawal *et al.* 2009; Varade *et al.* 2015). This reason seems not sufficient in rarefied gas flow, especially for a concave vortex, which may occur even when *Re* approaches zero, see figure 4(*a*). The underlying reason for the concave vortex and the additional reason for the convex vortex are the change of flow velocity due to the rarefaction effect characterised by the Knudsen number. From figure 8 we see that the slip velocity is also affected by the Knudsen number: at the concave corner, it increases with increasing *Kn*, while at the convex corner it decreases with increasing *Kn*. As a consequence, in agreement with the role of velocity slip on vortex formation as analysed in § 3.2, both types of vortices become smaller with increasing *Kn* at a fixed pressure ratio. Here, the concave and convex vortices start to disappear when the Knudsen number increases to 0.04 and 0.01, respectively.
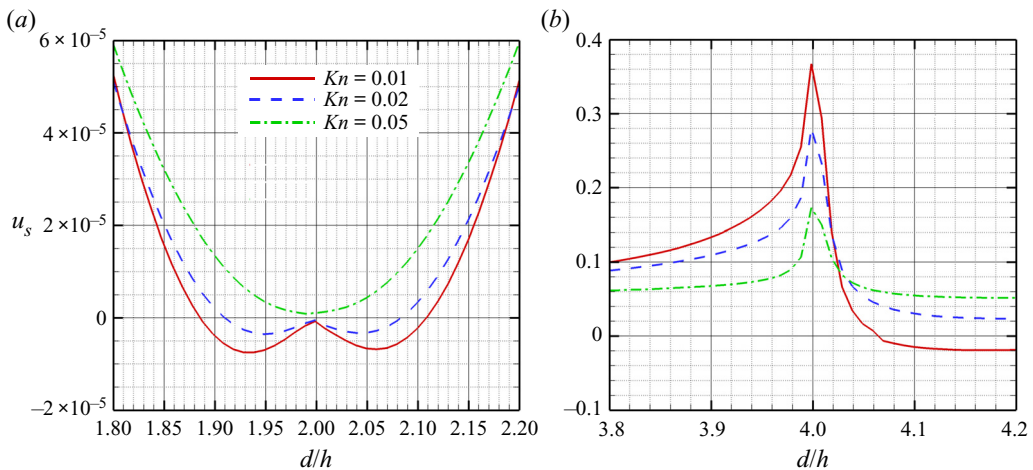
FIGURE 8. Influence of the Knudsen number on the slip velocity near (*a*) the first concave corner (the upper wall, $d/h = 2$) for $\beta = 0.99$, (*b*) the second convex corner (the upper wall, $d/h = 4$) for $\beta = 0.5$. The distance d is measured along the upper wall, starting from the inlet of the microchannel.

The adverse pressure gradient along the channel walls, which can be conveniently detected by pressure sensors (Lee *et al.* 2001; Varade *et al.* 2015), is usually used as an indicator for flow separation at bends. From our numerical data, adverse pressure gradients at both the concave and convex corners are reduced when the Knudsen number (Reynolds number) increases (decreases). The adverse pressure gradient along the concave wall exists in all the examined Re and Kn, while the adverse pressure gradient along the convex wall can only be found when $Kn \leq 0.1$, regardless of the pressure ratio β. However, the existence of adverse pressure gradient along the wall does not guarantee the flow separation as it may not lead to vortex generation. For example, although an adverse pressure gradient does occur at both the concave and convex corners for the case of pressure ratio $\beta = 0.5$ and $Kn = 0.05$ as shown in figure 3(*f*), no flow separation is found for this case.

4. Gain and loss of flow rate due to bend

Figure 9(*a*) summarises the ratio of reduced mass flow rate $\alpha = G_{bent}/G_{straight}$ as a function of Knudsen number at different pressure ratios β. In general, when the Knudsen number is fixed, a higher flow rate ratio is achieved with a larger pressure ratio β. This is because, with a fixed Kn, Re decreases with increasing β, which leads to a smaller adverse pressure gradient and/or a weaker vortex near the bend. Therefore, the kinetic energy loss becomes smaller. When the pressure ratio is fixed, the flow rate ratio reaches a maximum value slightly higher than unity in the slip flow regime. This maximum value increases and its location is shifted to smaller Kn when the pressure ratio β increases. With further decrease of Kn from the maximum point of α, the flow rate ratio reduces rapidly, and the smaller the pressure ratio, the steeper the reduction of mass flow rate. As a consequence, for larger values of β, not only is the gain of flow rate due to the bends more significant, but also occurs in a wider range of Kn, covering the continuum, slip and early transitional flow regimes. The maximum gain of flow rate is 2.8 %, 4.6 %, 8.2 % and 9.6 % at $Kn = 0.5, 0.4, 0.01$ and $10^{-5} \sim 2 \times 10^{-4}$ with $\beta = 0.5, 0.75, 0.99$ and
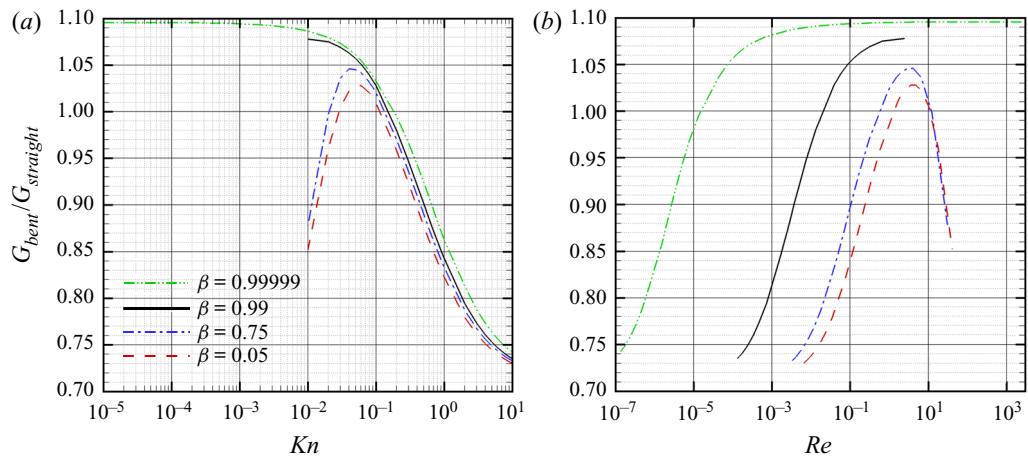
FIGURE 9. The ratio of reduced mass flow rate $\alpha = G_{bent}/G_{straight}$ versus (*a*) the Knudsen number, (*b*) the Reynolds number, at different pressure ratio β. (*a*) α versus Kn; (*b*) α versus Re.

0.99999, respectively. On the other hand, when the Knudsen number increases from the point where α is maximum, the mass flow rate ratio rapidly reduces with increasing Kn; also, the curves with different values of pressure ratio β tend to converge in the free-molecular flow regime. The maximum loss of flow rate due to the bends is approximately 27 % in the free-molecular flow regime.

It can also be seen in figure 9(*b*) that the maximum value of α occurs around $Re = 3.5$ for all β, where neither vortex nor significant adverse pressure gradients appear near the convex corner (see figure 3). So friction energy loss at the convex corner is comparable to that in a straight channel. By contrast, the friction energy loss at the concave corner is reduced significantly due to the suppressed shear stress (see figures 5*c* and 5*d*, in which the slip velocity is expected to be proportional to the shear stress according to Maxwell's slip velocity model), which is responsible for the flow rate gain in the channel with bends. The large decrease of shear stress and slip velocity near the concave corner was also observed in White *et al.* (2013) and Rovenskaya (2016) for the cases in which flow rate gain was found. When Re increases, the kinetic energy loss increases rapidly due to the development of adverse pressure gradient and vortices at both the convex and concave corners, so the reduction in friction energy loss cannot eventually compensate this kinetic energy loss, leading to a reduced flow rate ratio in comparison with a straight channel.

On the other hand, Re decreases with increasing Kn when β is fixed. A larger Kn leads to a more significant portion of flow rate contributed by velocity slip at the walls (Gu & Emerson 2009). However, unlike the straight channel, the slip in a bent microchannel is not always in the same direction as the mainstream, which may disturb and even weaken the main flow stream, thus resulting in a steep decline of flow rate ratio in flow with a large Kn.

Therefore, as shown in figure 9, the mass flow rate ratio strongly depends on both the Knudsen and Reynolds numbers. This can explain why the scattered values of α are found in the literature, see the summary in table 1, where a wide range of Kn and Re are covered.

5. Conclusions

In summary, we have simulated the rarefied gas flow through a microchannel with double rectangular bends connecting two large reservoirs over a wide range of Knudsen

numbers (from 10^{-4} to 10) and Reynolds numbers (from 10^{-7} to 10^3) and have found two types of flow separation near the concave and convex corners of the bends. The concave vortex, which is attributed to the Moffatt eddies, is found to shrink with the increase of the Knudsen number and slip velocity. This means that, compared with the continuum flow described by the Navier–Stokes equations with the no-slip velocity boundary condition, 'late onset' in terms of *Re* for the concave separation occurs in rarefied flow. When the Reynolds number is less than unity, the size of the Moffatt vortices is approximately 10 % of the channel height or less, so it is much more difficult to detect the Moffatt vortices in microsystems compared with macrosystems. In the literature, the concave vortex is only captured in rarefied gas flow at Reynolds number of the order of unity with a refined spatial grid (Agrawal *et al.* 2009; White *et al.* 2013; Varade *et al.* 2015). In this study, the concave vortex is found at *Re* as small as 0.32×10^{-3} due to the use of very refined spatial grids. Convex separation, which is attributed to the rapid turn of stream with large momentum passing through the convex corner, is found to be enhanced by slip velocity, resulting in 'early onset' of convex separation. This explains why the convex separation can occur at a much smaller critical Reynolds number (30.8 in the present case) in a rarefied flow.

Although adverse pressure gradients are respectively found at the convex and concave corners for $Kn \leq 0.1$ and all the examined *Kn*, they do not always indicate flow separation, which is different from the continuum flow because the flow is also affected by rarefaction. As the slip velocity near the concave/convex corner increases/decreases with the increase of *Kn*, both types of vortices are suppressed by increasing *Kn*. The concave and convex vortices are found to disappear when the Knudsen number is beyond 0.04 and 0.01, respectively. Compared with the straight channel of the same length, the bent channel may yield higher mass flow rate in the early transitional regime than in the continuum regime, due to a significant reduction of friction loss on the concave walls.

Scattered values of mass flow rate ratio reported in the literature can be explained by the following two factors. First, the mass flow rate ratio itself depends strongly on both *Kn* and *Re*. Second, the formation of secondary flow near a bend in a rarefied flow is largely affected by the slip velocity on the wall, so an appropriate model and fine spatial grids should be used to resolve the Knudsen layer at the wall surface in order to evaluate the performance of microchannel flows.

Acknowledgements

Declaration of interests

The authors report no conflict of interest.

Appendix A. Numerical validation

Convergence tests on molecular velocity grids and spatial grids used in this study have been performed to ensure that the change in mass flow rate is within 1 % when the number of grid points is doubled.
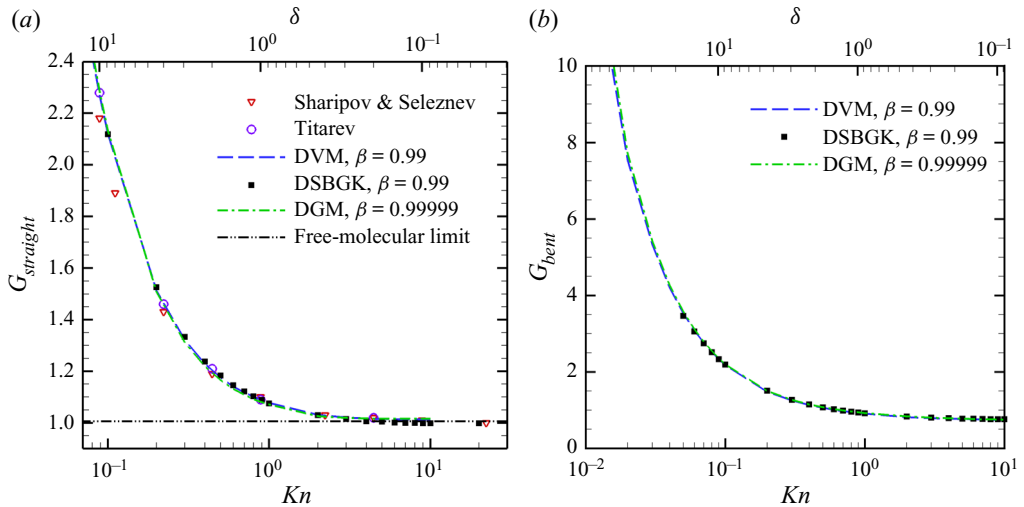
FIGURE 10. The reduced mass flow rate obtained by the DVM, DGM and direct simulation Bhatnagar–Gross–Krook (DSBGK) simulations: (*a*) straight channel, compared with the numerical data (Sharipov & Seleznev 1998; Titarev 2012*b*) and the analytical solution in the free-molecular flow regime using the Berman equation (A 1); (*b*) bent channel, cross-validation between the two numerical methods.

Figure 10(*a*) shows the dependence of reduced mass flow rate $G_{straight}$ on Kn for the straight channel. The reduced mass flow rate $G_{straight}$ reduces rapidly with increasing Kn in the slip-flow regime, then gradually decreases with increasing Kn in the transition-flow regime and finally reaches a plateau in the free molecular regime. The analytical solution for the straight channel of finite length in the free-molecular regime, i.e. $Kn = \infty$, is obtained by Berman (1966)

$$\left.\begin{array}{l} G_{straight}\left(Kn \to \infty\right) = \dfrac{1}{\sqrt{\pi}} Q l_{ch}, \\[4mm] Q = 0.5\left(1 + \sqrt{1 + l_{ch}^2} - l_{ch}\right) - 1.5 \dfrac{\left[l_{ch} - \ln\left(l_{ch} + \sqrt{1 + l_{ch}^2}\right)\right]^2}{l_{ch}^3 + 3l_{ch}^2 + 4 - \left(l_{ch}^2 + 4\right)\sqrt{1 + l_{ch}^2}}, \end{array}\right\} \quad (A\,1)$$

where Q and $l_{ch} = L_{ch}/h$ are the transmission probability and dimensionless length of the channel, respectively.

The DGM and DVM data are almost identical except for small deviations around $Kn = 1$. Our numerical results are also in good agreement with the numerical data of Sharipov & Seleznev (1998) and Titarev (2012*b*) for $Kn \geq 0.5$. At lower Kn, our numerical data are in very good agreement with Titarev's data and considerably higher than Sharipov and Seleznev's results. This can be attributed to the insufficient grid resolution used more than 20 years ago in Sharipov and Seleznev's work. Relative fine grid resolution was used in Titarev's work and our $G_{straight}$ of the grid $L20W8d80$ being higher than that of the grid $L20W8d40$. It is noted that the linearised Bhatnagar–Gross–Krook model and linearised Shakhov model were used in Sharipov and Seleznev's work and Titarev's work, respectively. In the present work, we solve both the linearised and nonlinear Shakhov models. The DGM and DVM results are further compared with results obtained by the DSBGK method (Li 2011; Ho *et al.* 2019; Li 2020). The DSBGK simulations use the

grid $L20W16h20$ for $Kn \geq 1$ and the grid $L10W8h40$ for $Kn < 1$ as the mass flow rate for cases of relatively small pressure drop is of interest. Very good agreement can be observed between the three numerical methods.

Figure 10(*b*) shows the reduced mass flow rate G_{bent} as a function of Kn for the bent channel with pressure ratio $\beta = 0.99$ and $\beta = 0.99999$. Our DGM, DVM and DSBGK data are in very good agreement. The interested reader is referred to Ho *et al.* (2019) and Su *et al.* (2020*a*) for more information about the computational performance of our methods.

REFERENCES

AGRAWAL, A., DJENIDI, L. & AGRAWAL, A. 2009 Simulation of gas flow in microchannels with a single 90° bend. *Comput. Fluids* **38** (8), 1629–1637.

BERMAN, A. S. 1966 Erratum: free molecule transmission probabilities. *J. Appl. Phys.* **37** (12), 4598.

BIRD, G. A. 1994 *Molecular Gas Dynamics and the Direct Simulation of Gas Flows*. Oxford University Press.

BISWAS, G., BREUER, M. & DURST, F. 2004 Backward-facing step flows for various expansion ratios at low and moderate Reynolds numbers. *Trans. ASME: J. Fluids Engng* **126** (3), 362–374.

BRADSHAW, P. & WONG, F. Y. F. 1972 The reattachment and relaxation of a turbulent shear layer. *J. Fluid Mech.* **52** (1), 113–135.

BROADWELL, J. E. 1964 Study of rarefied shear flow by the discrete velocity method. *J. Fluid Mech.* **19** (3), 401–414.

BURGGRAF, O. R. 1966 Analytical and numerical studies of the structure of steady separated flows. *J. Fluid Mech.* **24** (1), 113–151.

GU, X. J. & EMERSON, D. R. 2009 A high-order moment approach for capturing non-equilibrium phenomena in the transition regime. *J. Fluid Mech.* **636**, 177–216.

HO, M. T. & GRAUR, I. 2014 Numerical study of unsteady rarefied gas flow through an orifice. *Vacuum* **109**, 253–265.

HO, M. T., LI, J., WU, L., REESE, J. M. & ZHANG, Y. 2019 A comparative study of the DSBGK and DVM methods for low-speed rarefied gas flows. *Comput. Fluids* **181**, 143–159.

KULAKARNI, N. K., SHTEREV, K. & STEFANOV, S. K. 2015 Effects of finite distance between a pair of opposite transversal dimensions in microchannel configurations: DSMC analysis in transitional regime. *Intl J. Heat Mass Transfer* **85**, 568–576.

LEE, S. Y. K., WONG, M. & ZOHAR, Y. 2001 Gas flow in microchannels with bends. *J. Micromech. Microengng* **11** (6), 635–644.

LI, J. 2011 Direct simulation method based on BGK equation. In *Proceedings of the 27th International Symposium on Rarefied Gas Dynamics* (ed. D. A. Levin, I. J. Wysong & A. L. Garcia), vol. 1333, pp. 283–288. AIP.

LI, J. 2020 *Multiscale and Multiphysics Flow Simulations of Using the Boltzmann Equation*. Springer.

LIU, W., TANG, G., SU, W., WU, L. & ZHANG, Y. 2018 Rarefaction throttling effect: influence of the bend in micro-channel gaseous flow. *Phys. Fluids* **30** (8), 082002.

LOYALKA, S. K. 1968 Momentum and temperature-slip coefficients with arbitrary accommodation at the surface. *J. Chem. Phys.* **48** (12), 5432–5436.

MAHARUDRAYYA, S., JAYANTI, S. & DESHPANDE, A. P. 2004 Pressure losses in laminar flow through serpentine channels in fuel cell stacks. *J. Power Sources* **138** (1–2), 1–13.

MOFFATT, H. K. 1964 Viscous and resistive eddies near a sharp corner. *J. Fluid Mech.* **18** (1), 1–18.

RAJU, R. & ROY, S. 2004 Hydrodynamic model for microscale flows in a channel with two 90 deg bends. *J. Fluids Engng* **126** (3), 489–492.

ROVENSKAYA, O. I. 2016 Computational study of 3D rarefied gas flow in microchannel with 90 bend. *Eur. J. Mech.* B/*Fluids* **59**, 7–17.

SAZHIN, O. 2009 Rarefied gas flow through a channel of finite length into a vacuum. *J. Expl Theor. Phys.* **109** (4), 700–706.

SHAKHOV, E. M. 1968 Generalization of the Krook kinetic relaxation equation. *Fluid Dyn.* **3** (5), 95–96.

SHARIPOV, F. 2004 Numerical simulation of rarefied gas flow through a thin orifice. *J. Fluid Mech.* **518**, 35–60.

SHARIPOV, F. & GRAUR, I. A. 2012 Rarefied gas flow through a zigzag channel. *Vacuum* **86** (11), 1778–1782.

SHARIPOV, F. & SELEZNEV, V. 1998 Data on internal rarefied gas flows. *J. Phys. Chem. Ref. Data* **27** (3), 657–706.

SU, W., HO, M. T., ZHANG, Y. & WU, L. 2020*a* GSIS: an efficient and accurate numerical method to obtain the apparent gas permeability of porous media. *Comput. Fluids* **206**, 104576.

SU, W., WANG, P., LIU, H. & WU, L. 2019*a* Accurate and efficient computation of the Boltzmann equation for Couette flow: influence of intermolecular potentials on Knudsen layer function and viscous slip coefficient. *J. Comput. Phys.* **378**, 573–590.

SU, W., WANG, P., ZHANG, Y. & WU, L. 2019*b* A high-order hybridizable discontinuous Galerkin method with fast convergence to steady-state solutions of the gas kinetic equation. *J. Comput. Phys.* **376**, 973–991.

SU, W., ZHU, L., WANG, P., ZHANG, Y. & WU, L. 2020*b* Can we find steady-state solutions to multiscale rarefied gas flows within dozens of iterations? *J. Comput. Phys.* **407**, 109245.

TITAREV, V. A. 2007 Conservative numerical methods for model kinetic equations. *Comput. Fluids* **36** (9), 1446–1459.

TITAREV, V. A. 2012*a* Implicit high-order method for calculating rarefied gas flow in a planar microchannel. *J. Comput. Phys.* **231** (1), 109–134.

TITAREV, V. A. 2012*b* Rarefied gas flow in a planar channel caused by arbitrary pressure and temperature drops. *Intl J. Heat Mass Transfer* **55** (21-22), 5916–5930.

TITAREV, V. A. 2013 Rarefied gas flow in a circular pipe of finite length. *Vacuum* **94**, 92–103.

VALOUGEORGIS, D. & NARIS, S. 2003 Acceleration schemes of the discrete velocity method: gaseous flows in rectangular microchannels. *SIAM J. Sci. Comput.* **25** (2), 534–552.

VARADE, V., AGRAWAL, A., PRABHU, S. V. & PRADEEP, A. M. 2015 Early onset of flow separation with rarefied gas flowing in a 90° bend tube. *Exp. Therm. Fluid Sci.* **66**, 221–234.

VAROUTIS, S., DAY, C. & SHARIPOV, F. 2012 Rarefied gas flow through channels of finite length at various pressure ratios. *Vacuum* **86** (12), 1952–1959.

WANG, M. & LI, Z. 2004 Simulations for gas flows in microgeometries using the direct simulation Monte Carlo method. *Intl J. Heat Fluid Flow* **25** (6), 975–985.

WANG, P., HO, M. T., WU, L., GUO, Z. & ZHANG, Y. 2018 A comparative study of discrete velocity methods for low-speed rarefied gas flows. *Comput. Fluids* **161**, 33–46.

WHITE, C., BORG, M. K., SCANLON, T. J. & REESE, J. M. 2013 A DSMC investigation of gas flows in micro-channels with bends. *Comput. Fluids* **71**, 261–271.

XIONG, R. & CHUNG, J. N. 2008 Effects of miter bend on pressure drop and flow structure in micro-fluidic channels. *Intl J. Heat Mass Transfer* **51** (11-12), 2914–2924.

YANG, J. Y. & HUANG, J. C. 1995 Rarefied flow computations using nonlinear model Boltzmann equations. *J. Comput. Phys.* **120** (2), 323–339.